Electronic Supplementary Material (ESI) for RSC Advances.

Supporting Information

Visible-Light-Driven CO_2 Reduction on Dye-Sensitized NiO Photocathodes Decorated with Palladium Nanoparticles

Ewelina Szaniawska,[a] Anna Wadas,[a] Hasina H. Ramanitra,[b] Emmanuel A. Fodeke,[b] Kamila Brzozowska,[a] Alexandre Chevillot-Biraud,[b] Marie-Pierre Santoni,[b,] Iwona A. Rutkowska,[a,*] Mohamed Jouini[b], and Pawel J. Kulesza[a*]*

[a] Faculty of Chemistry, University of Warsaw, Pasteura 1, PL-02-093 Warsaw, Poland

[b] Université de Paris, ITODYS, CNRS, F-75006 Paris, France

1. Electrochemical and spectroscopic properties of P1 dye

Table S1. Data for electronic and redox properties of dye P1 in solution (P. Qin, *et al., J. Am. Chem. Soc*. 2008, **130**, 8570-8571).

Compound	**λ_{max} (nm) (ε, $M^{-1}.cm^{-1}$)**	**$E_{0\text{-}0}$ (eV)**	**E(D/D-) (V)**	**E(D*/D-) (V)**	**HOMO (V*vs. RHE*)**	**LUMO (V*vs. NHE*)**
Dye P1 (D)	468 (58000)	2.25	-1.00 *vs. SCE* -0.46 *vs. RHE*	+1.25 *vs. SCE* +1.79 *vs. RHE*	+1.38	-0.87

A qualitative control experiment was performed to confirm that the process observed around -0.6 V *vs. RHE* on the photoelectrodes is the reduction of P1 to $P1^-$. The cyclic voltamogramm of the obtained modified GC electrode was recorded in deoxygenated 0.1 mol dm^{-3} Na_2SO_4 (Figure S1): the reduction of P1 to $P1^-$ is observed at Ered = -0.54 V *vs. RHE* (-1.19 V *vs. SCE*).

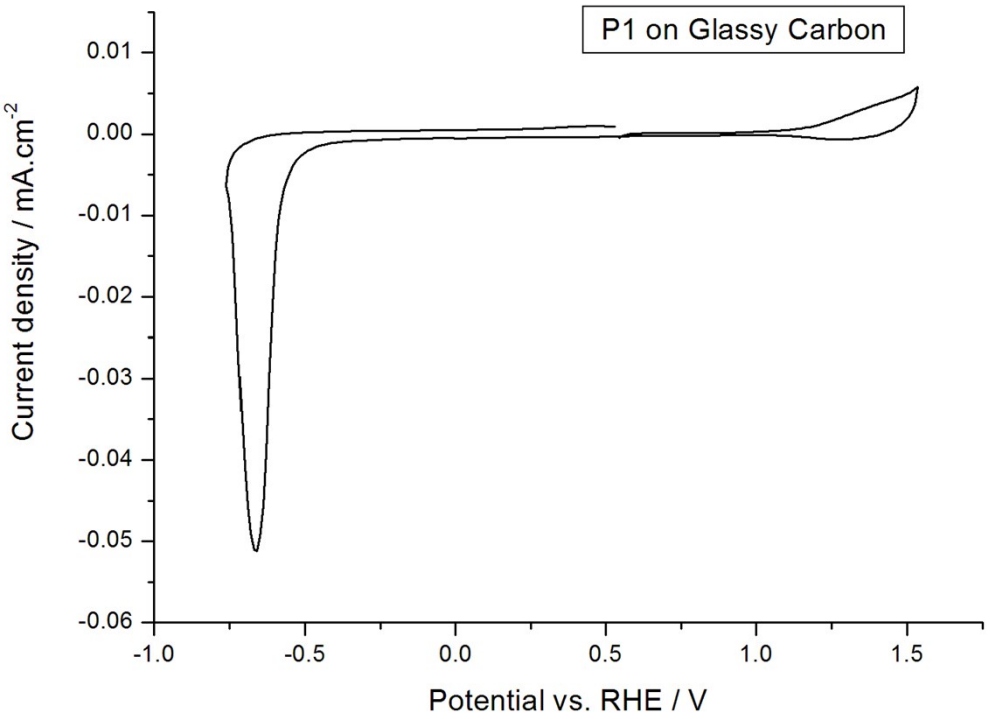

Fig. S1. Cyclic voltammogram for P1 drop-casted on GC (glassy carbon), recorded in deoxygenated 0.1 mol dm^{-3} Na_2SO_4. Counter-electrode: a stainless-steel grid. Scan rate: 50 $mV.s^{-1}$.

2. Crystal structure of NiO

The crystal structure of bunsenite NiO (cubic phase, space group *F*m-3m) has been reported (ICSD-53930, for example, see A. Leineweber, H. Jacobs, S. Hull, *Inorg. Chem.*, 2001, **40**, 5818-5822). The (002) and (111) crystallographic planes seem to be predominant over the (022) planes in the mesoporous layer. The closely-packed face-centered arrangement (Figure S2) of the *bunsenite* phase is known to possess two types of channels within the crystal structure. The smaller channel is observed along the *a* axis and has a maximum cross-section surface of: $(2.091)^2/4 = 1.09$ Å^2. The wider channel is observed along the *a*+*b* axis and has a maximum cross-section surface of: $(2.958)^2/4 = 2.19$ Å^2. Surfaces are here roughly estimated for information (regarding doping/de-doping redox processes), without consideration of Van der Waals atomic radii. These channels in the nanocrystalline NiO phase are not accessible to diffusing small molecules and ions from electrolyte. On the other hand, the mesoporous over-layer could allow some intercalation of small charge-compensating ions, as evidenced by reversible redox processes (oxidation of Ni centers at the interface with the electrolyte) and electrochromic properties.

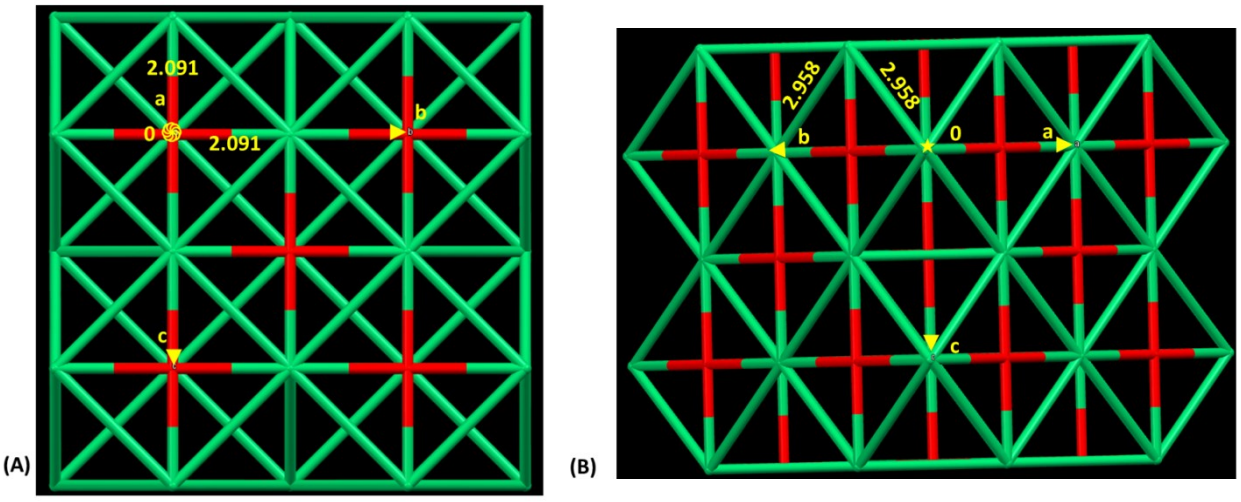

Fig. S2. Crystal packing of NiO bunsenite, showing the two types of channels present in the structure, along: (A) the *a* axis ([100]), smaller channels; (B) the *a*+*b* axis ([110]), wider channels.

3. Scanning Electron Microscopy characterization

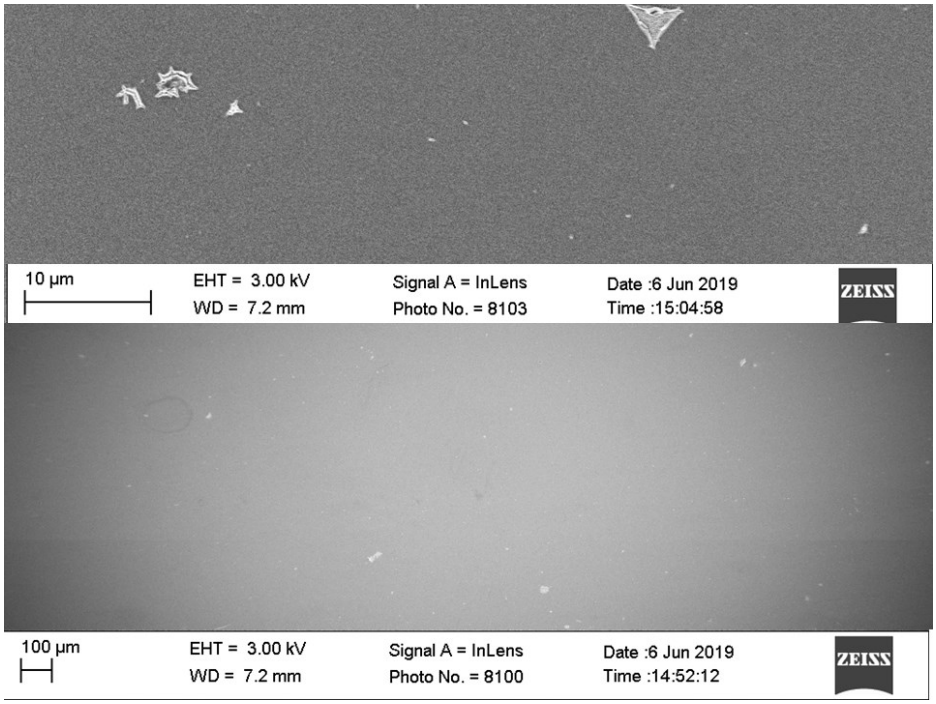

Fig. S3. Top-view SEM image of FTO/NiO (1 BL) electrode showing a rather homogeneous surface with some surface defects (cracks).

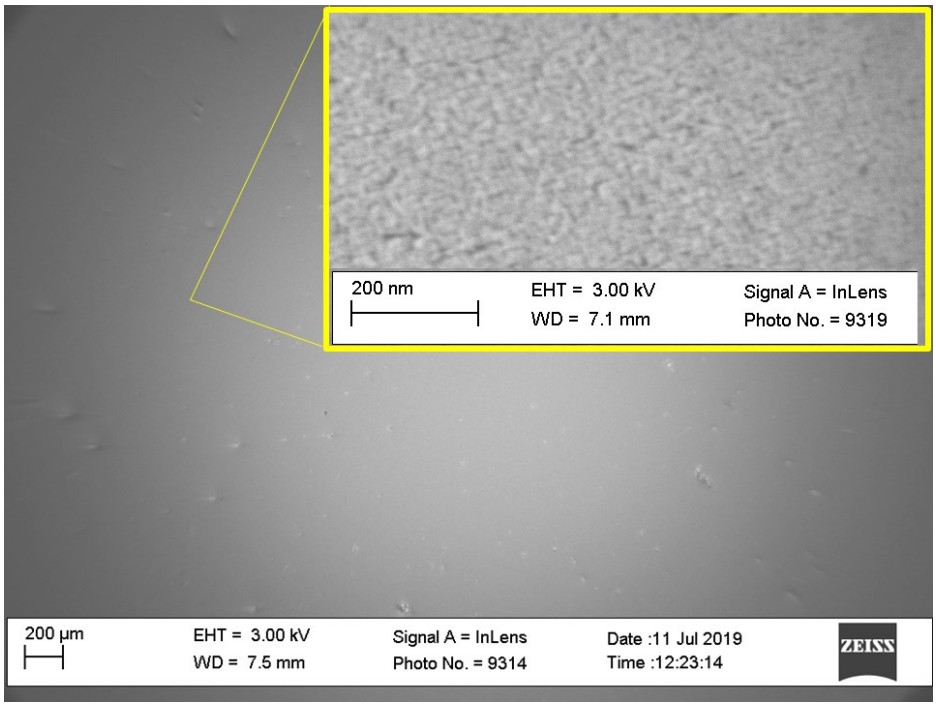

Fig. S4. Top-view SEM image of FTO/NiO (mesoporous) electrode showing a rather homogeneous surface with some surface defects (cracks).

4. Electrochemical characterization of FTO/NiO electrode

4.1. Cyclic Voltammetry

The first oxidation peak at 0.93 V (Fig. S5) shall be attributed to the oxidation of Ni(II) to Ni(III) accompanied by the release of proton:

$$Ni^{II}O(OH)_n(H_2O)_p \rightarrow Ni^{II}Ni^{III}O(OH)_{n+1}(H_2O)_{p-1} + e^- + H^+ \quad \text{[eq. 1]}$$

whereas the second oxidation peak at 1.26 shall be assigned to the oxidation of Ni(III) to Ni(IV)

$$Ni^{II}Ni^{III}O(OH)_{n+1}(H_2O)_{p-1} \rightarrow Ni^{II}Ni^{IV}O(OH)_{n+2}(H_2O)_{p-2} + e^- + H^+ \quad \text{[eq. 2]}$$

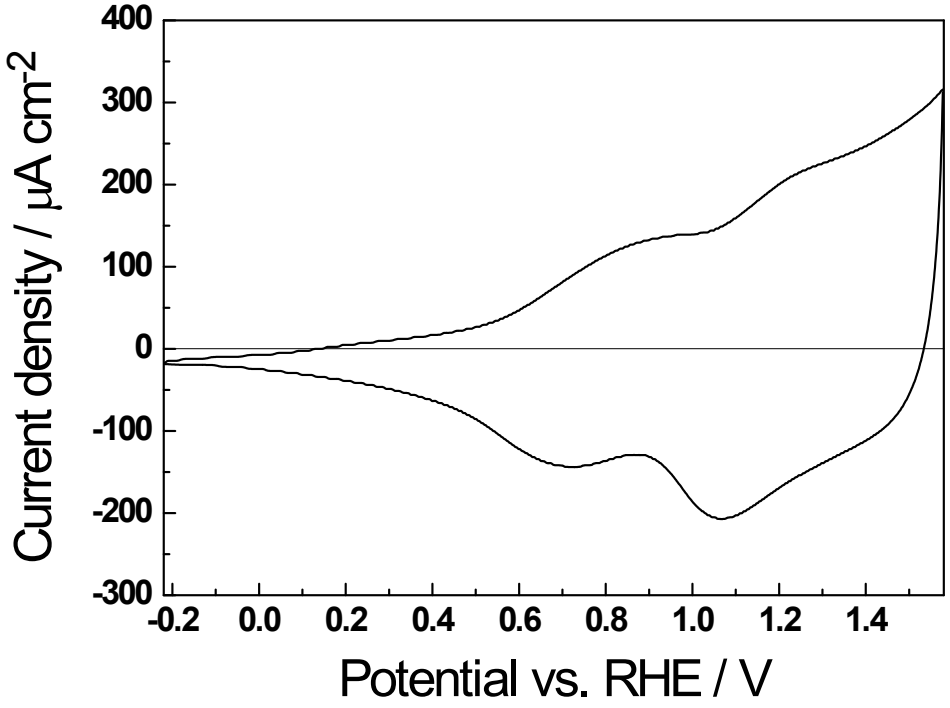

Fig. S5. Cyclic voltammetric response of mesoporous FTO/NiO recorded in de-oxygenated (argon-saturated) 0.1 mol dm^{-3} Na_2SO_4. Scan rate, 20 mV s^{-1}.

4.2. Square-Wave Voltammetry

As there was debate in the literature (E.A. Gibson, *et al. Phys. Chem. Chem. Phys.,* 2013, **15**, 2411-2420 and references therein.), Square-Wave Voltammetry experiments were performed in order to verify the number of electrons exchanged in the successive processes observed for the oxidation of NiO. Scanning from +1.54 V to -0.46 V *vs. RHE*, we observed two

monoelectronic processes (Figure S4): the calculated integrals for the processes centred at 0 V and 0.5 V are -32 720 and -44710 µA.V, respectively.

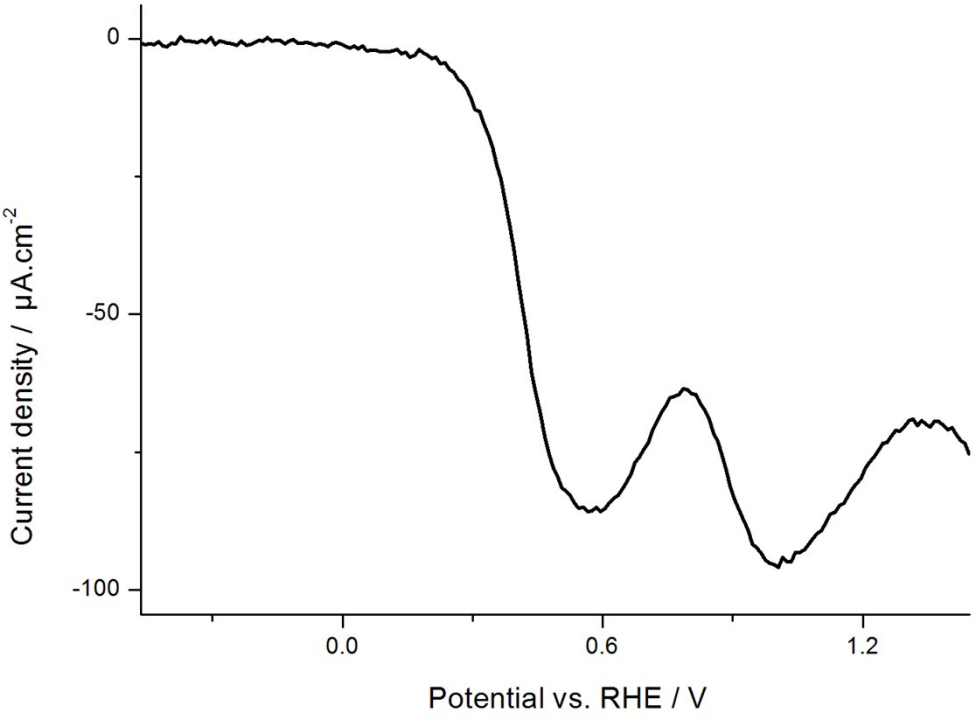

Fig. S6. Square-Wave Voltamogramm of mesoporous FTO/NiO electrode in deoxygenated 0.1 mol dm^{-3} Na_2SO_4(aq) (pulse height p_H = 2.50 mV, pulse width p_W = 500 ms, step height s_H = 10.00 mV).

5. Absorption of thin mesoporous films

5.1. FTO/NiO and Tauc plot

In order to confirm the optical band gap of the synthesized NiO mesoporous thin films, the UV-Vis absorption of FTO/NiO was substracted from the FTO contribution and the Tauc plot was drawn (inset in Fig. S6). The band gap energy Eg can be estimated using the Tauc relationship (here for direct transitions in thin films – see (a) S.M., Sze, K.K. Ng, *Physics of Semiconductor Devices*, 3rd edition, Wiley, New Jersey, 2007; (b) D.L. Wood, J. Tauc, *Phys. Chem. Rev. B*, 1972, **5**, 3144-3151):

$(\alpha h\nu)^n = A(h\nu - Eg)$ where α is the absorption coefficient, $h\nu$ is the incident photon energy, A is a constant, n = 2 for direct transitions. The calculation was made with a film thickness of 600 nm (in agreement with SEM imaging). We mention here that consideration direct (n=2) and indirect (n=1/2) transitions gave, in both cases, a linear fit for $(\alpha h\nu)^n$ (for indirect, band gap Eg = 3.5 eV). We chose to consider the direct transitions as NiO samples are transparent thin films (600 nm).

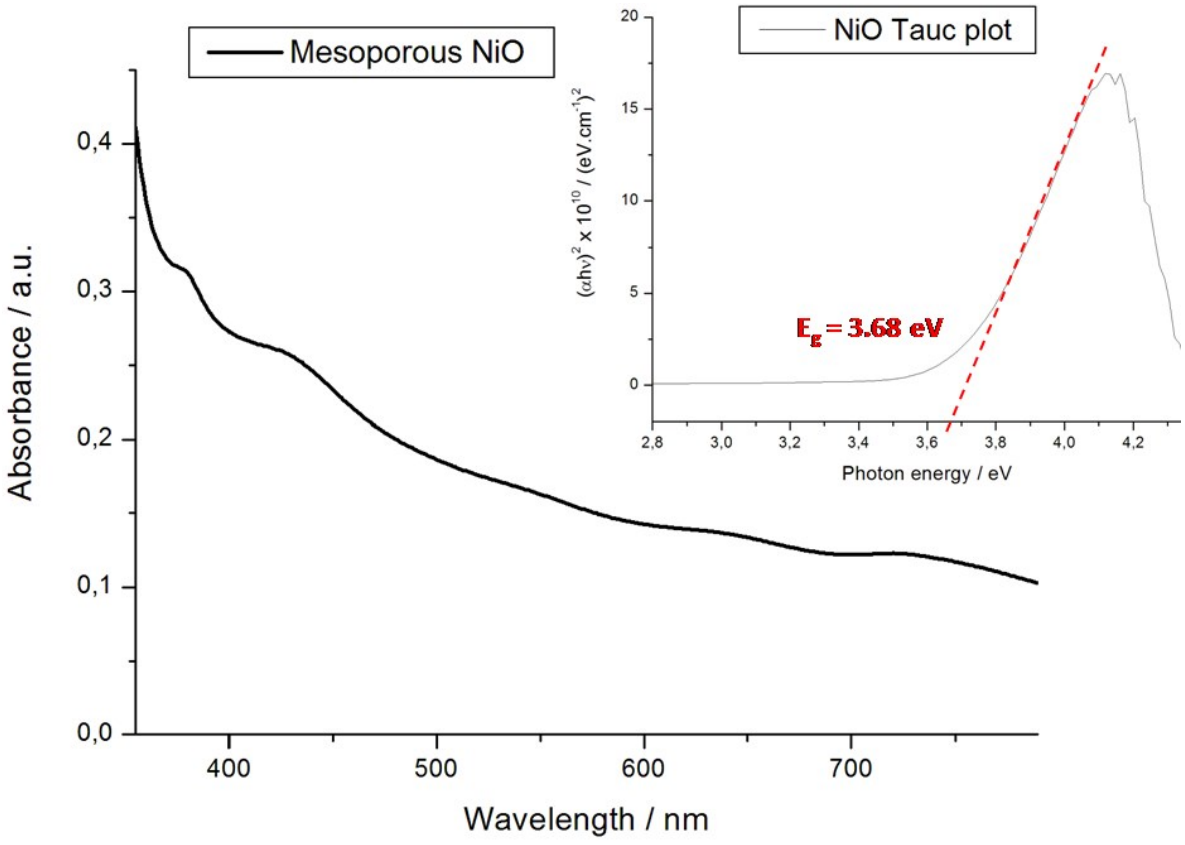

Fig. S7. UV-Vis absorption spectrum of NiO thin film; inset is the Tauc plot, confirming an optical band gap (direct) of 3.68 eV.

5.2. FTO/NiO-P1

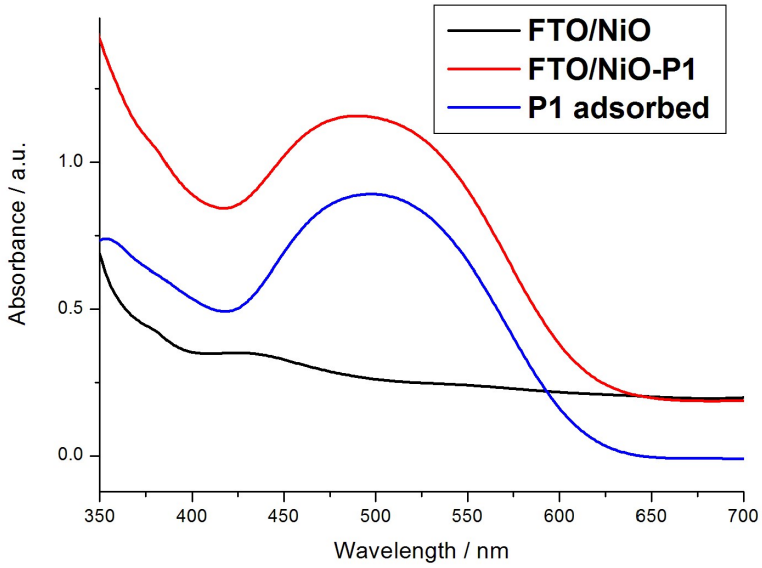

Fig. S8. Absorbance UV-visible spectra of NiO film (deposited on FTO) measured before and after sensitization with P1-dye.

6. Nyqvist plots

- **FTO/NiO electrode under Ar**

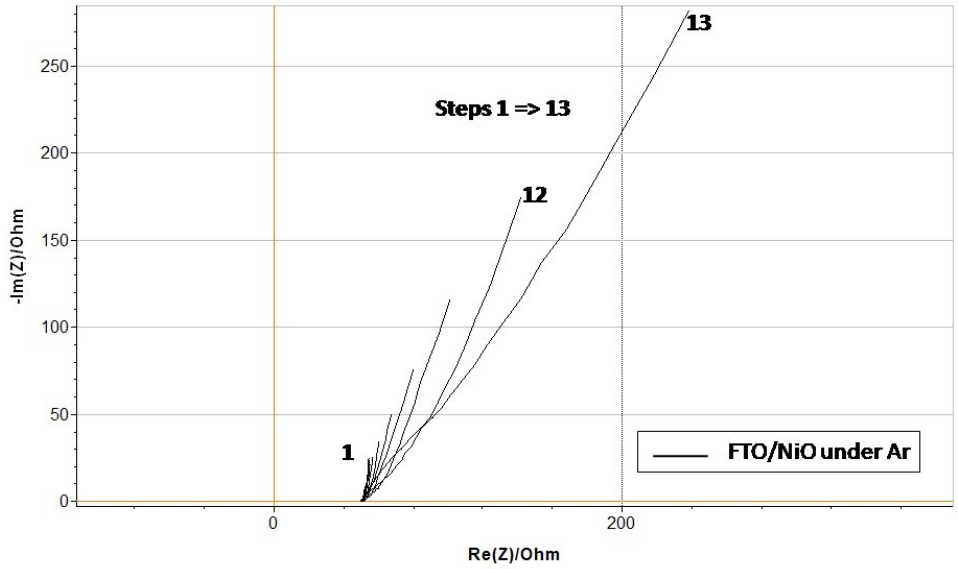

Fig. S9. Nyqvist plot for FTO/NiO electrode in 0.1 mol dm^{-3} Na_2SO_4 under Ar.

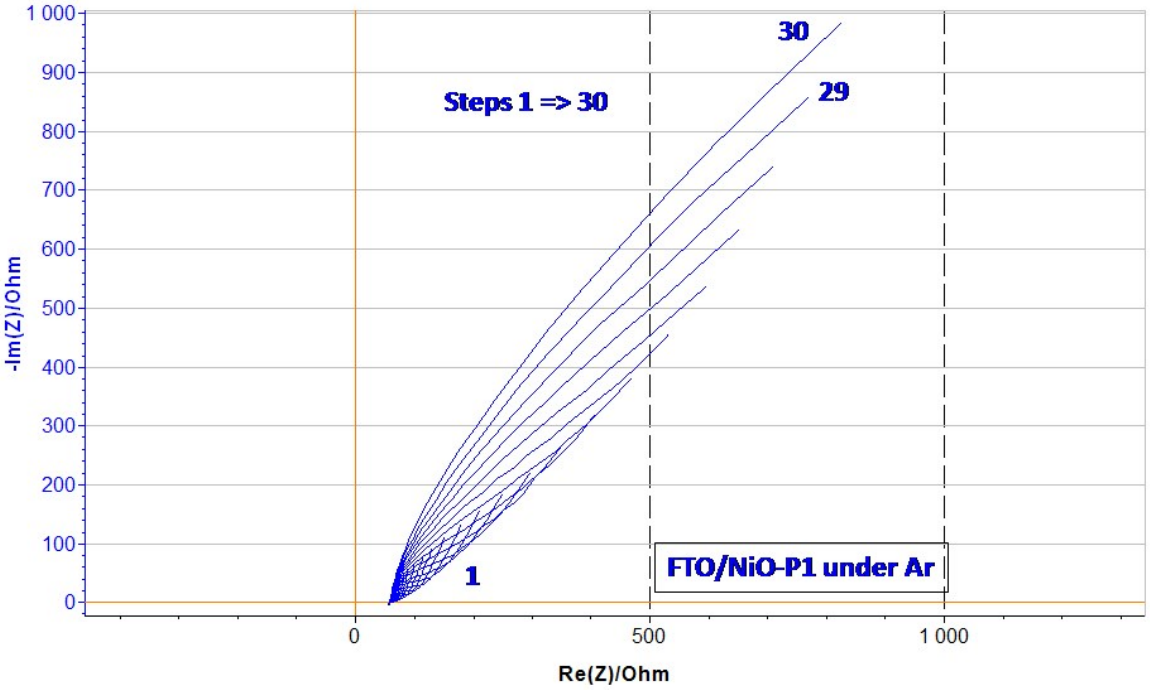

Fig. S10. Nyqvist plot for FTO/NiO-P1 electrode in 0.1 mol dm^{-3} Na_2SO_4 under Ar.

7. Mott-Schottky plots

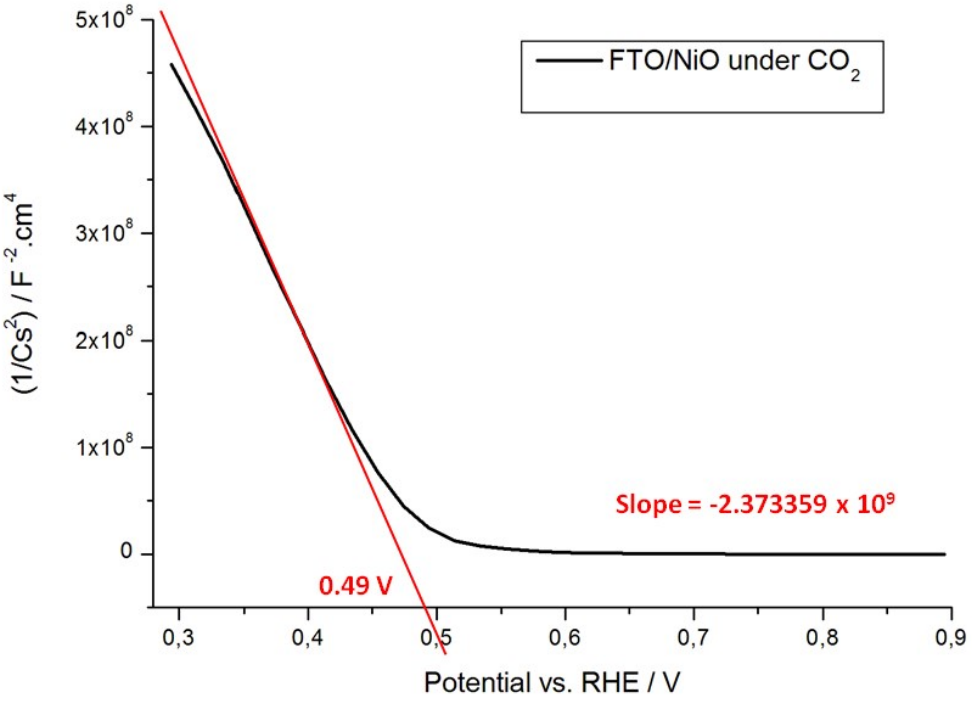

Fig. S11. Mott-Schottky plot for FTO/NiO electrode in 0.1 mol dm^{-3} Na_2SO_4 under CO_2 and determination of the flat band potential.

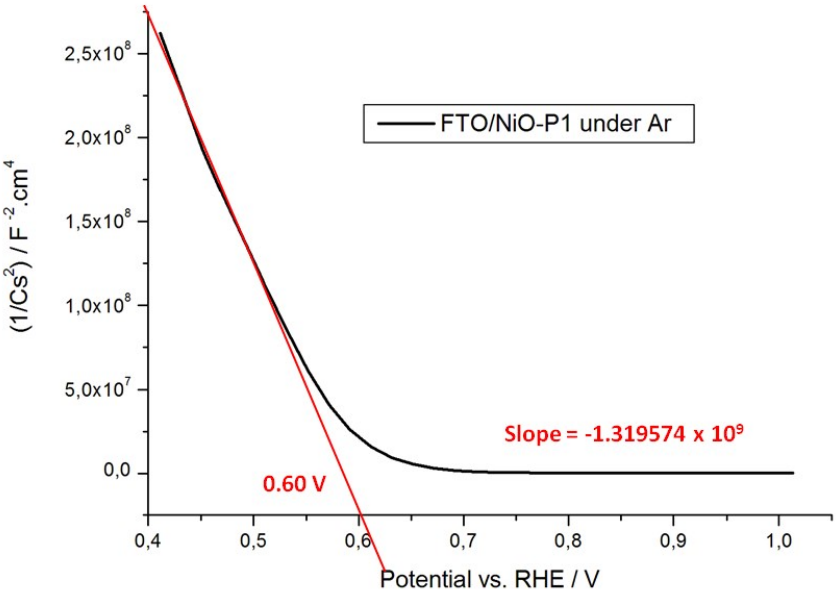

Fig. S12. Mott-Schottky plot for FTO/NiO-P1 electrode 0.1 mol dm^{-3} Na_2SO_4 under Ar and determination of the flat band potential.

8. Decoration with Pd nanoparticles

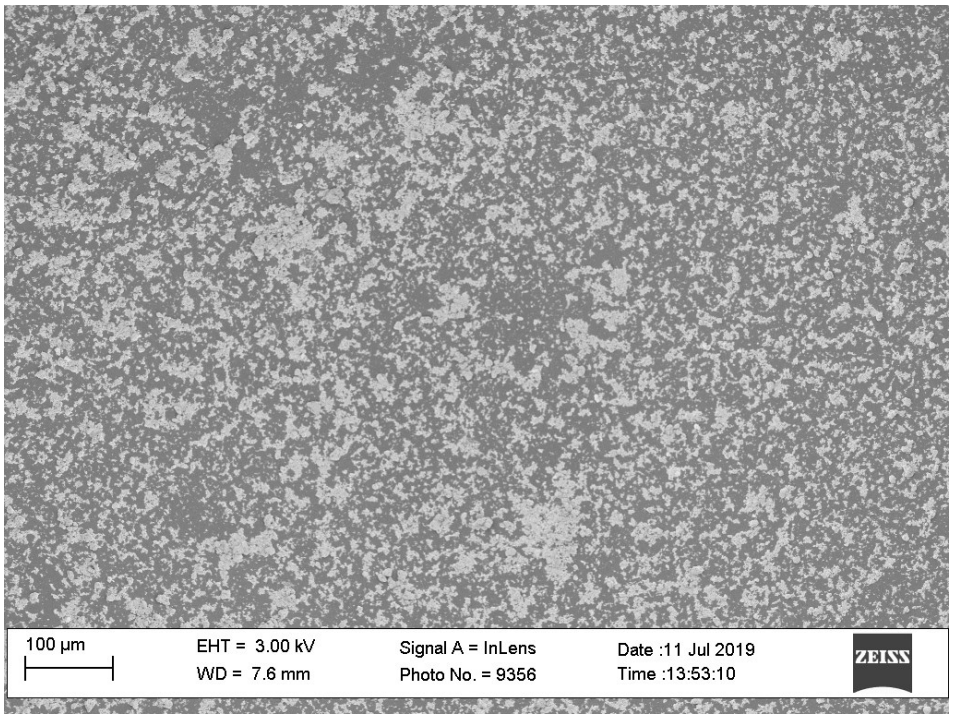

Fig. S13. Top-view SEM image of FTO/NiO-P1/nPd electrode before catalysis. Aggregates of nPd are seen (lighter color) on the NiO-P1 surface (large section shown).

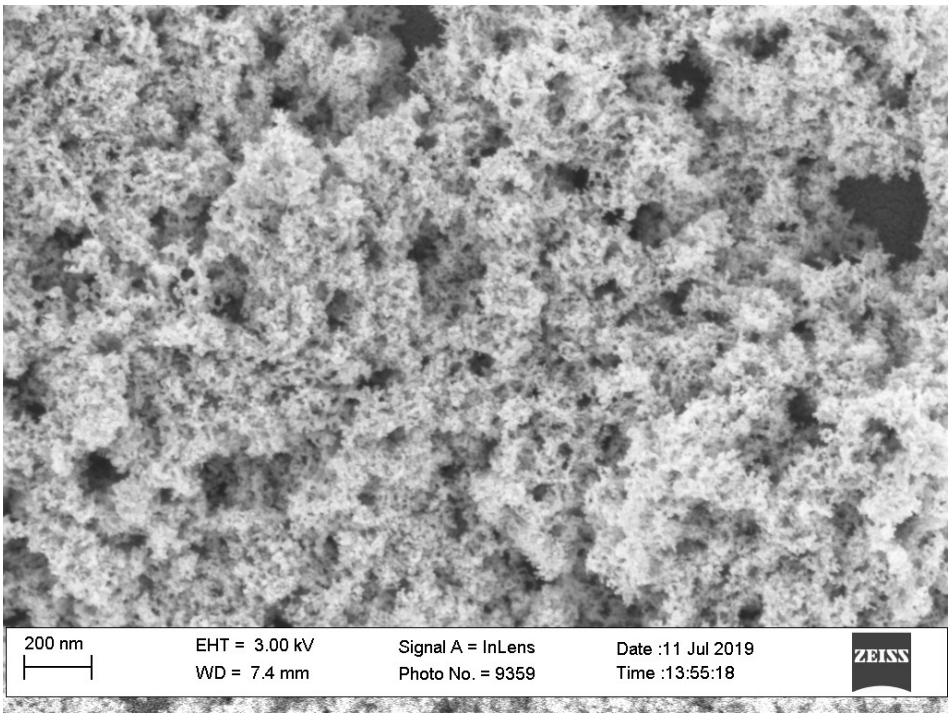

Fig. S14. Top-view SEM image of FTO/NiO-P1/nPd electrode before catalysis. A closer image of nPd aggregates deposited on the NiO-P1 surface displays the porous structure of aggregates formed by small nanoparticles (~6-10 nm) and the active surface area available for catalysis.

9. Photoelectrochemical performance of FTO/NiO-based systems

9.1. Cyclic voltammetry

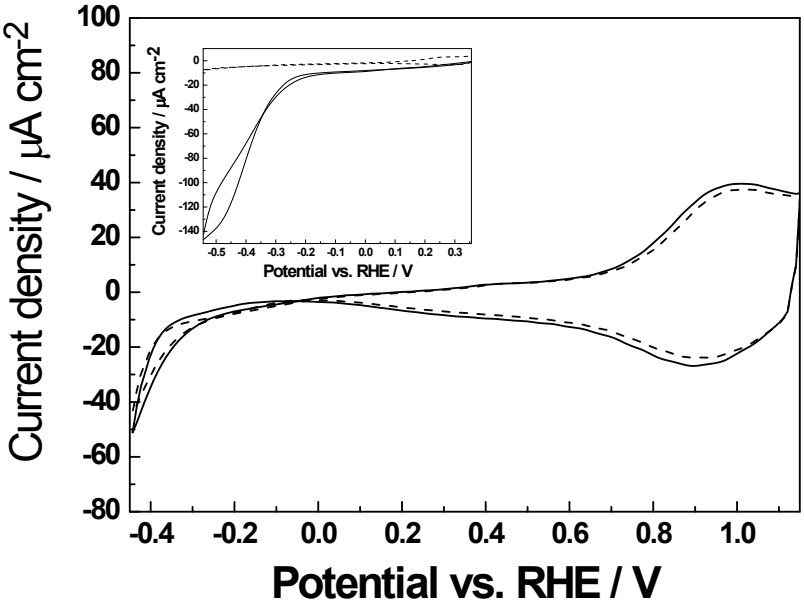

Fig. S15. Cyclic voltammetric responses recorded for FTO/NiO in 0.1 mol dm^{-3} Na_2SO_4 saturated with CO_2: in dark (solid line) and upon illumination with AM 0.1G filter (dashed line). Scan rate, 20 mV s^{-1}. Inset illustrates conventional (no illumination) voltammetric behavior of FTO/NiO in the presence (solid line) and absence (dashed line) of CO_2.

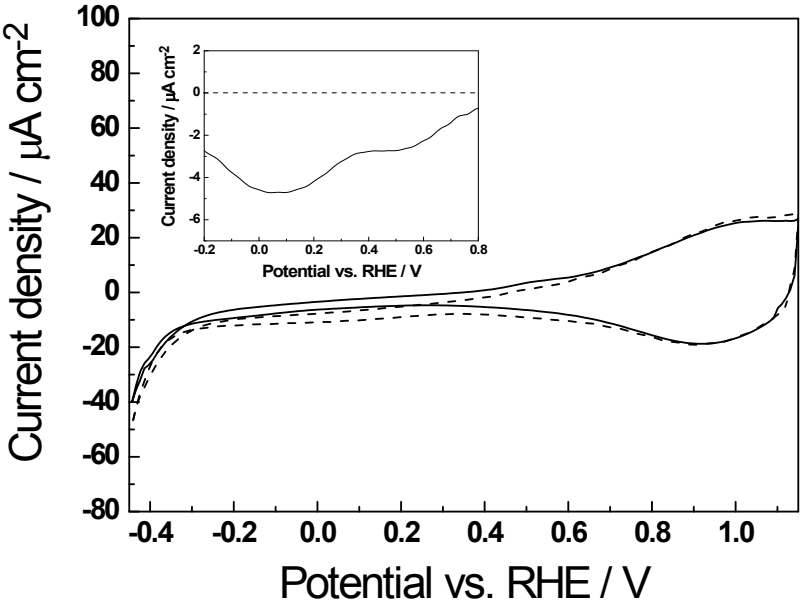

Fig. S16. Cyclic voltammograms recorded for FTO/NiO-P1 in 0.1mol dm^{-3} Na_2SO_4 saturated with CO_2: in dark (solid line), and upon illumination with AM 0.1G filter (dashed line). Scan rate, 20 mV s^{-1}. Inset illustrates the net current (i.e., dark-background-current-subtracted) density response obtained upon irradiation (solid line).

9.2. Details for verification of reaction products using anodic stripping voltammetry

In order to identify the products formed during catalysis, an additional glassy carbon working electrode (with deposited Pt nanoparticles; loading 100 μg cm^{-2}) has been introduced to the measurement cell and placed in the vicinity (ca. 0.5 cm apart) of the photocathode. After long-term photoelectrochemical reduction of CO_2 at the FTO/NiO-P1/nPd(x1) electrode (performed under the same experimental conditions than the ones used in Fig. 5A, except for chronoamperometry using a bias potential of -0.6 V), the photogenerated reaction products have been adsorbed and pre-concentrated (upon application of 0.34 V) on surfaces of Pt nanoparticles existing on the additional glassy carbon electrode. By choosing the pre-concentration potential value more positive than 0.25 V, namely 0.34 V, *i.e.*, outside the range characteristic of the formation of hydrogen adsorption peaks on Pt, care has been exercised to avoid interference originating from the reduction of CO_2 (existing in the reaction medium) on Pt. Consequently, no additional reduction products would be adsorbed on platinum during the pre-concentration step at 0.34 V. Later, the electrode has been transferred to deoxygenated 0.5 mol dm^{-3} (separate solution) to execute the actual stripping-type voltammetric oxidation experiment (Fig. 7). Although the latter stripping step can also be performed in the near-neutral Na_2SO_4 electrolyte,[72] voltammetric patterns characteristic of electrocatalytic oxidations of the adsorbates of small organic molecules are more unequivocal in acid medium.

10. Concept of photocathode:Step-by-step preparation (layer-by-layer assembly)

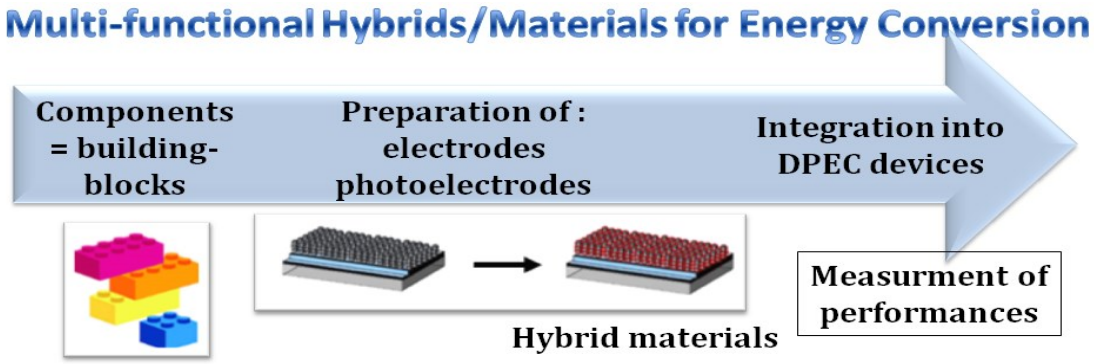

Fig. S17. Step-by-step preparation and assembly of a dye-sensitized photoelectrochemical (DPEC) device: (1) the tunable assembly of functional components (building blocks: dye, catalyst) into hybrid electrode and photoelectrode materials; (2) integration of photoelectrodes into DPEC devices for measurement of performances and insights into better understanding and optimization of processes.